

Article

Effect of Chloride and Corrosion of Reinforcing Steel on Thermal Behavior of Concrete and its Modeling

David Im^{1,a}, Pakawat Sancharoen^{2,b,*}, Parnthep Julnipitawong²,
and Somnuk Tangtermsirikul³

¹ School of Civil Engineering and Technology (CET), Sirindhorn International Institute of Technology (SIIT), Thammasat University, Thailand

² Construction and Maintenance Technology Research Center (CONTEC), School of Civil Engineering and Technology (CET), Sirindhorn International Institute of Technology (SIIT), Thammasat University, Thailand

³ School of Civil Engineering and Technology (CET), Sirindhorn International Institute of Technology (SIIT), Thammasat University, Thailand

E-mail: ^aim_david07@yahoo.com, ^bpakawat@siit.tu.ac.th (Corresponding author)

Abstract. Chloride induced corrosion of reinforcing steel is a significant problem. Thermograph is one of the Non-Destructive Testing methods which may be useful for detecting corroded bar in reinforced concrete. This study aims to investigate the thermal behavior of concrete influenced by chloride and corrosion of reinforcing steel. The results of this thermal behavior are useful for determining the detectability of corrosion by thermograph. Different mix proportions of concrete and level of corrosion were studied. The results of temperature profiles obtained from experimental work proved that when there is presence of dense rust confined between concrete and steel, thermal behavior of concrete around steel bar changed. When applying heat source on top surface of the specimen, there was a slight change of temperature on top of corroded bar while there was more signification change of temperature below it. This is because dense rust with low porosity is a better heat conductor when compared to concrete. The temperature history obtained from simulation and experiment are in a good agreement. Numerical simulation provides quite good results in the area closing to the concrete top surface (depth 0.5cm and 1.5cm) and the accuracy of the estimated temperature is within 2%-5% of the experimental results.

Keywords: Corrosion, thermal properties, FEM analysis, specific heat, thermal conductivity.

ENGINEERING JOURNAL Volume 22 Issue 3

Received 4 August 2017

Accepted 19 March 2018

Published 28 June 2018

Online at <http://www.engj.org/>

DOI:10.4186/ej.2018.22.3.143

1. Introduction

For many decades, concrete has become the most significant material for the world infrastructure development. Since concrete structures are suffering to the chloride attack and the fact that this aggressive ion is the main factor to break down the passive layer of concrete, thus the corrosion of embedded steel bars inside concrete will consequently be accelerated [1, 2]. Carbonation is another phenomenon that causes rebar corrosion. In term of concrete deterioration, chloride induced corrosion of reinforcing steel inside concrete remains the most significant issue. That is why a proper inspection and maintenance planning is required for ensuring structural performance and safety. Many researchers have been trying to develop non-destructive techniques to determine the existent of steel corrosion and precisely estimate the amount of corrosion. Half-cell potential was developed to evaluate the corrosion of steel reinforcement based on the electrochemical process [3, 4]. However, this technique provides a limited information and is also applicable only to a small area of inspection. On the other hand, application of thermograph in Non-Destructive Testing (NDT) have been used widely in civil engineering filed. The principle of this technique is mainly based on difference of thermal properties of investigated materials. It is typically used to observe the propagation of heat in materials while they are heating up or cooling down. Since the defective area of the inspected materials are strongly affected by the diffusion of heat it may appear to be hotter or cooler than non-defective area or sound areas [5]. Maierhofer., et al. [6], studied the application of Impulse-thermography to inspect the void underneath the concrete surface with the influence of various material properties such as age of concrete, pore content, aggregate type and reinforcement density. The results of the studied indicated that the application of thermograph can detect the surface-near void of concrete. However, the detectability is low when there is presence of porous aggregates or high density of reinforcement. To quickly evaluate the extension of corrosion of reinforcing steel, infrared thermography is proposed, as a Non-Destructive Testing method, based theoretically on the different thermal behavior of the non-corroded and corroded reinforced concrete. The main principle in term of thermal behavior is that the corroded steel bar produces rust on the surface of the steel bar which influences the heat transfer and may influence the surface temperature of the concrete.

This paper aims to study the effect of corrosion and chloride on thermal properties and also the possibility of using infrared thermography to detect corrosion of reinforcing steel before cracking and spalling so that the early problem can be identified before it becomes more serious. To achieve this objective, experiments were conducted to investigate relevant parameters affecting the detectability of active thermography, including concrete mix proportion and corrosion amount. Numerical analysis was also conducted to further simulate the thermal behavior by considering related elements including rust in the concrete pores and steel bar interfacial zone.

2. Materials and Methodology of the Study

2.1. Concrete Mix Proportions and Materials

This study was also focused on the influence of concrete mixtures which have different thermal properties and eventually lead to different heat transfer mechanism. The mix proportions in this study were both Ordinary Portland Cement (OPC I) concrete and Fly Ash (Mae Moh Fly Ash) replacement concrete, with two different water to binder ratios. The tested mix proportions are shown in Table 1, Table 2, and Table 3 summarize the properties of the materials used for the mix proportioning.

Table 1. Concrete mix proportion.

Mix No.	Number Specimens	w/b	Fly replacement ratio (%)	Ash	Unit Content (kg/m ³)					
					Cement	FA	Water	Sand (SSD)	Gravel (SSD)	Admixture Type F
w4r0	2	0.4	0		435	0	174	746	1101	2.2
w6r0	2	0.6	0		340	0	204	746	1101	0
w4r3	2	0.4	30		295	126	169	746	1101	1.09
w6r3	2	0.6	30		233	100	199	746	1101	0

Remarks: w/b = water to binder ratio, FA = Fly Ash.

Table 2. Chemical compositions and physical properties of ordinary Portland cement type I and Fly ash.

Materials	SiO ₂ (%)	Al ₂ O ₃ (%)	Fe ₂ O ₃ (%)	CaO (%)	MgO (%)	SO ₃ (%)	LOI (%)	Blaine (cm ² /g)	Fineness	Specific gravity
OPC I	19.70	5.19	3.34	64.80	1.20	2.54	2.10	3100		3.15
Fly Ash	26.61	13.60	18.344	24.97	2.33	8.53	0.53	2820		2.57

Table 3. Physical properties of aggregates.

Properties	Fine aggregate	Coarse aggregate
Type of aggregate	River sand	Crushed limestone
Specific gravity (g/cm ³)	2.62	2.80
Absorption (%)	1.16	0.82
Maximum size (mm)	4.75	19
Finesses modulus	2.84	3.98

2.2. Specimens Preparation

Reinforced concrete specimens with the size 200mm×400mm×100mm, having a deformed reinforcing bar grade SD40 with a diameter of 16mm and 240mm in length were cast. Thermocouples type K were installed at four different depths, 5mm, 15mm, 40mm and 75mm from the top surface, to investigate the temperature distribution during test. The set of thermocouples were installed at 2 positions, at the center (line C in Fig. 1(a) and Fig. 1(b)) and at 10 cm far from the rebar (line S in Fig. 1(a) and Fig. 1(b)). This purpose was to avoid the boundary effect and more importantly for checking the detectability of Infrared thermograph on corrosion of embedded reinforcing steel by investigating thermal contrast. In order to simulate heat transfer in a real structure having much larger size than the prepared specimens, all concrete specimen surfaces, except the top surface, were covered by 1 inch thickness of styrofoam to prevent heat loss. An overview detail of specimen is shown in Fig. 1.

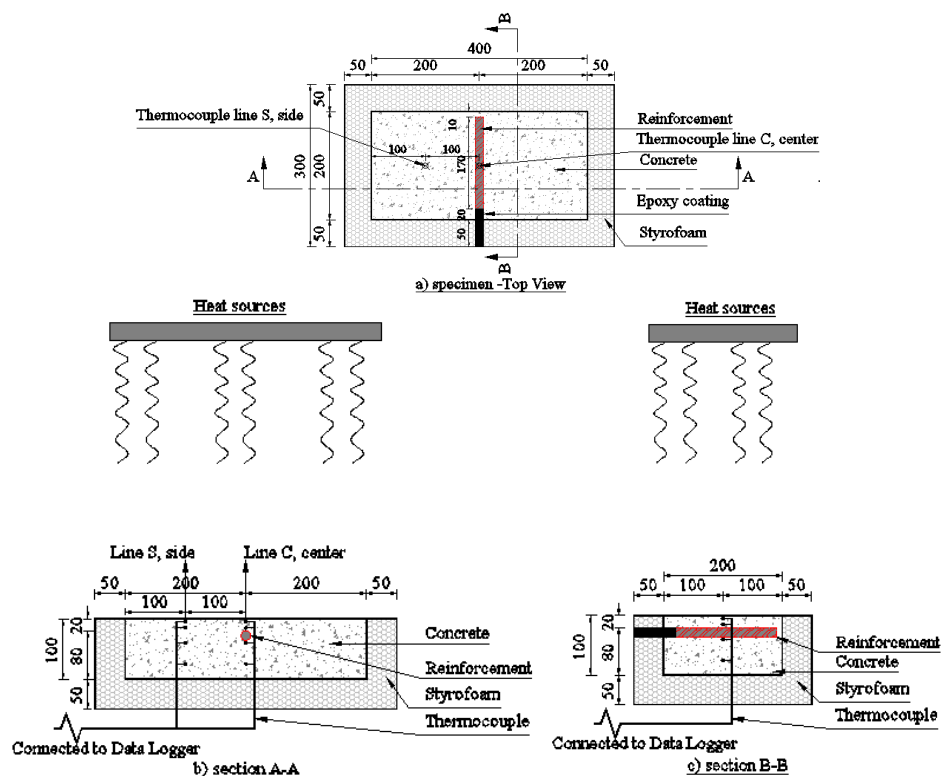


Fig. 1. Specimens for corrosion detection with covering depth (unit: mm).

Two specimens were prepared for each mix proportion. One specimen was selected to be the control specimen with no corrosion while another was used to process corrosion at different levels. Variation of corrosion levels of embedded reinforcing steels in corroded specimens was operated by applying an impressed current method [7]. At approximately 24 hours after casting, each specimen was removed from the mold and cured in a water tank for 28 days.

2.3. Corrosion acceleration by impressed current method

To accelerate the corrosion of the embedded steel bars, the impressed current method was applied as detailed in Fig. 2. The impressed current method consists of a DC power source, a counter electrode and an electrolyte. A positive electric wire of DC source is connected to an end of the reinforcing steel and acts as the anode while the negative electric wire is connected to the stainless steel mesh as the cathode. The concrete specimens were put in a tank containing 5% sodium chloride solution (NaCl). Only about the thickness of the concrete cover depth of each specimen was immersed in the solution (see section A-A in Fig. 2). This concept helps to migrate the chloride and oxygen ions into the concrete specimen so that the anodic and cathodic reactions occur and corrosion products can be generated. With adjustable DC voltage supply, the current was adjusted to maintain the required current density for accelerating the corrosion process. Following the Faraday's law, the amount of mass loss are computed as expressed in Eq. (1):

$$M_{th} = \frac{W \times I_{app} \times T}{F} \quad (1)$$

where M_{th} is the computed mass of rust per unit surface area of steel bar (g/cm^2), W is the equivalent weight of steel (27.925g), I_{app} is the applied current density (Amp/cm^2), T is the duration of induced corrosion (sec) and F is Faraday's constant (96487 Amp.sec).

In this study, the current intensity of $1.17mA/cm^2$ was applied with different period of time to obtain the required levels of corrosion of 0.1%, 0.19%, 0.39%, 0.78% and 1.16% by weight of steel (%bws) as shown in Table 4. The percentage of mass loss is calculated as the ratio of computed mass loss to the initial mass of steel.

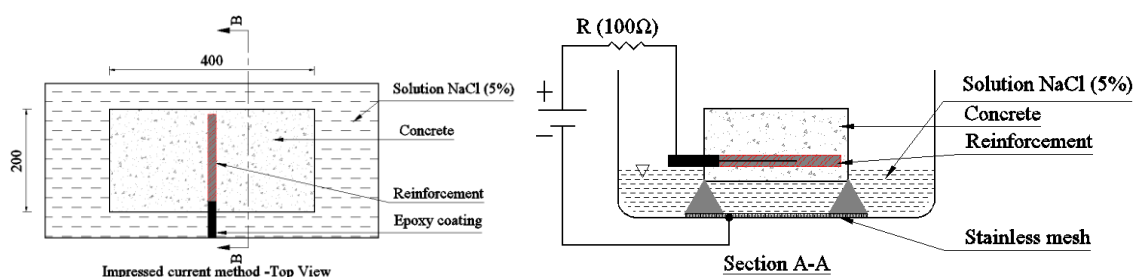


Fig. 2. Set up of impressed current method for corrosion acceleration.

Table 4. Condition for impressed current method for corrosion acceleration.

Specimen type	Initial mass of steel (g/cm^2)	Impressed current density (mA/cm^2)	Time for induced corrosion (h)	NaCl solution (%by weight)	Computed mass loss (mg/cm^2)	Percentage of mass loss (% by weight of steel)
Corroded	3.14	1.17	2.5	5	3.05	0.10
		1.17	5	5	6.10	0.19
		1.17	10	5	12.19	0.39
		1.17	20	5	24.38	0.78
		1.17	30	5	36.57	1.16

2.4. Testing

2.4.1. Heating and cooling

To enable the comparison between temperature profiles of corroded and non-corroded specimens, two specimens for each mix proportion, control and corroded, were subjected to the same heat source and heating time. The external thermal excitation was operated with a commercial infrared heater having 3000W of heating capacity. The distance from the surface of the test specimens and the infrared heater was fixed at 0.5 m. Each test was carried out for four hours which was split into two phases, heating and cooling, lasting two hours for each phase. Fig. 3 shows the equipment and specimen set up during the heating and cooling periods.



Fig. 3. Equipment and specimen set up for measuring temperature profile.

2.4.2. Thermocouple measurement

During heating and cooling, the embedded thermocouples at different positions and depths were connected to the data logger and the temperature inside the concrete specimens were recorded at every one minute.

The obtained data were used to plot the transient temperature curves with time. This transient temperature curve is beneficial to analyze the thermal characteristics of the test specimens. Since the starting point of initial temperature of each specimen could be different, so to avoid the effect of initial temperature and clearly observes the temperature profile, the obtained data were used to analyze and plot the transient temperature rise curve, as shown in Eq. (2). However, it should be noted here that condition of ambient temperature in the test room was almost the same for all tested cases (see Fig. 4).

$$\Delta T = T(t) - T(t=0) \quad (2)$$

where ΔT is the temperature rise ($^{\circ}\text{C}$), $T(t)$ is the temperature at time t (min), and $T(t=0)$ is the initial temperature at starting time of measurement ($^{\circ}\text{C}$).

In the study of corrosion detection of embedded reinforcing steel, the thermal contrast based technique is adopted. The definition of thermal contrast is basically defined as the surface temperature difference ($\Delta T_{\text{contrast}}(t)$) between a defective zone ($T_{\text{def}}(t)$) and a non-defective zone or sound area ($T_{\text{sa}}(t)$) at a certain time, as shown in Eq. (3):

$$\Delta T_{\text{contrast}}(t) = T_{\text{def}}(t) - T_{\text{sa}}(t) \quad (3)$$

Furthermore, this study also aimed to check for the effect of corrosion product on the temperature characteristics of reinforced concrete. Thus, the different temperature ($\Delta T_{\text{diff}}(t)$) between temperature of corroded and non-corroded specimen was investigated as expressed in Eq. (4)

$$\Delta T_{\text{diff}}(t) = \Delta T_{\text{corroded}}(t) - \Delta T_{\text{non-corroded}}(t) \quad (4)$$

where $\Delta T_{\text{corroded}}(t)$ is the temperature rise of corroded specimen ($^{\circ}\text{C}$) and $\Delta T_{\text{non-corroded}}(t)$ is the temperature rise of non-corroded specimen ($^{\circ}\text{C}$).

2.4.3. Ambient temperature

Ambient temperature variation during the temperature recording period of all specimens were recorded and it is clearly shown Fig. 4 that they are almost identical. This ambient temperature history was used as an input in the analysis.

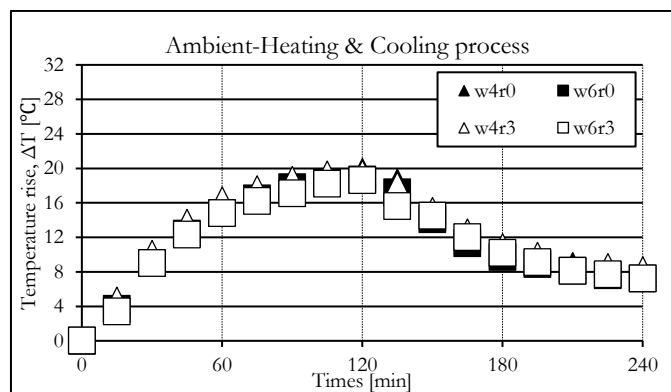


Fig. 4. Ambient temperature in the test room.

3. Numerical Simulation

The numerical simulation modeling in this study was conducted with a commercial Finite element software, ANSYS. Version 17.2. The transient thermal analysis method was selected to simulate experimental program of this study. This analysis included all materials involved in the experimental work such as concrete, reinforcing steel, corrosion products (rust) and styrofoam. Thermal properties of each type of simulated elements were obtained from other researchers as shown in Table 5.

Table 5. Thermal properties of materials.

Specimen	Specific heat (J/kg. $^{\circ}\text{C}$)	Thermal Conductivity (W/m 2 . $^{\circ}\text{C}$)	References
w4r0	819.775	2.356	Choktaweekarn, P. [8]
w6r0	913.978	2.321	Choktaweekarn, P. [8]
w4r3	842.802	2.333	Choktaweekarn, P. [8]
w6r3	879.646	2.326	Choktaweekarn, P. [8]
Steel	460.55	51.3	Oshita, H. [9]
Rust	1200	0.07	Oshita, H. [9]
Styrofoam	1045	0.026	Michael, J.M. [10]

3.1. Modelling of Rust Elements

The modeling of corrosion products is established based on different levels of corrosion. Basically, corrosion does not only reduce the cross section but also increase the thickness of corrosion layer at the interfacial zone between concrete and steel [11]. Figure 5 illustrates the geometrical characteristics of concrete, steel bar and corrosion products. Figure 5 shows the dimensions of the initial radius of reinforcing steel (R_0), radius of reinforcing steel after corrosion (R_1), radius of reinforcing steel with rust thickness (R_2), corrosion penetration (X) and rust thickness (ΔR).

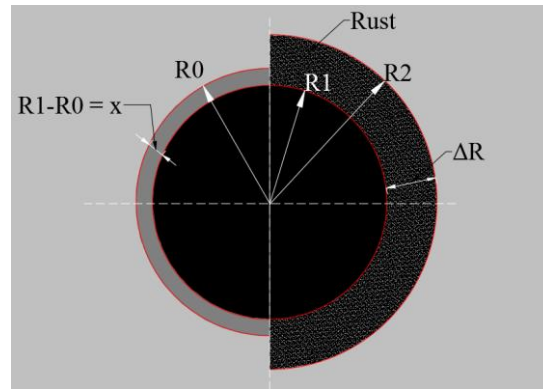


Fig. 5. Geometrical characteristics of concrete, steel and rust.

Assuming that the corrosion products is uniform on the reinforcing steel surface. Thus, in principle of Faraday's law, corrosion penetration (radius loss of steel bar) can be defined from each applied current which was 100% spent in the oxidation of the steel [12]. When rust attacks a cylindrical steel, the corrosion penetration can be calculated as expressed in Eq. (5).

$$X = \frac{M_{Fe} \cdot I_{corr} \cdot \Delta t}{\rho_{Fe} \cdot n \cdot F} \quad (5)$$

where X is the corrosion penetration (mm), M_{Fe} is the atomic mass of Fe ($56 \cdot 10^{-3}$ kg/mol), ρ_{Fe} is the unit weight of Fe (7850 kg/m³), n is the valence of Fe (2 or 3), F is Faraday's number (96500 C/mol), I_{corr} is the corrosion current density (μ A/cm²) and Δt is the test period (year). By substituting the known parameters, Eq. (6) becomes:

$$X = 0.0116 \times I_{corr} \times \Delta t \quad (6)$$

On the other hands, the volume expansion of corrosion products or rust thickness model was estimated based on the volumetric expansion ratio of corrosion products and steel which was assumed here to be 2.5 [13]. It is noted that this ratio can be different depending on the type of rust. So the rust layer thickness can be estimated as shown in Eq. (7).

$$\Delta R = \frac{\eta R_0 (\alpha_{corr} - 1)}{2} \quad (7)$$

Where ΔR is the rust thickness (mm), η is the percentage of mass loss (%bws), R_0 is the initial radius of steel (mm) and α_{corr} is the volumetric expansion ratio of corrosion products which is assumed to be 2.5 times of the original steel.

Table 6 shows the values of corrosion penetration and rust thickness at each percentage of mass loss which was calculated based on Eq. (6) and Eq. (7) and were further used as inputs in the numerical simulation.

Table 6. Corrosion penetration and rust thickness of corrosion products at each percentage of mass loss.

Specimen type	Diameter of rebar (mm)	Percentage of mass loss (%bws)	Corrosion penetration, x (mm)	Rust thickness, ΔR (mm)
Corroded specimen	16	0.10	0.00387	0.01165
		0.19	0.00775	0.02329
		0.39	0.01550	0.04659
		0.78	0.03099	0.09318
		1.16	0.04649	0.13977

3.2. Heat Flux

Heat flux was selected to simulate the external heat source from the Infrared heater. To validate the value of heat flux accurately, back analysis calculation was applied. In the principle of heat transfer, the rate of heat generation and its temperature rise is expressed as in Eq. (8):

$$Q_{sp} = \frac{mC_p\Delta T_{sp}}{A_s\Delta t} \quad (8)$$

where Q_{sp} is the total heat transferred into the element (W/m^2), m is the mass of element (kg), C_p is the specific heat of the element ($J/kg \cdot ^\circ C$), ΔT_{sp} is temperature rise of the element ($^\circ C$), A_s is the element surface area (m^2) and Δt is heating time (sec). Element of the object is defined according to Section 3.5.1.

Performing back calculation properly, the temperature rise of bare concrete section of the test specimens were used. Furthermore, the heating time, actual mass and surface of specimen were measured directly in the experimental program. Specific heat, on the other hands, was estimated as shown in Table 5.

3.3. Heat Convection

According to Newton's cooling law, as expressed in Eq. (9), the convective heat transfer in transient model does not only depend on the convective coefficient, h_c , but is also influenced by the surface temperature and ambient temperature. Therefore, with this relationship, the ambient temperature in Fig. 4 used as an input.

$$Q_{con} = A_s h_c (T_s - T_{air}) \quad (9)$$

where Q_{con} is heat flow from the surface into air (W), T_{air} is ambient air temperature ($^\circ C$), T_s is concrete surface temperature ($^\circ C$), A_s is the specimens surface (m^2) and h_c is the average convection heat transfer coefficient ($W/m^2 \cdot ^\circ C$) determined from Eq. (10) [14, 15].

$$h_c = 5.7 + 3.8V \quad (10)$$

where V is the wind speed (m/s). The experiments were carried out in a control room with no wind. Then the convection coefficient of heat transfer was constantly treated as $5.7 W/m^2 \cdot ^\circ C$.

3.4. Heat Radiation

Similar to heat convection, heat radiation emitted or absorbed by specimens has great interaction with the ambient temperature. Based on the Stefan-Boltzmann law, the rate of radiation heat transfer between the concrete and air is expressed in Eq. (11) [16].

$$Q_r = \epsilon \sigma A_s (T_s^4 - T_{air}^4) \quad (11)$$

where Q_r is emitting energy (W), ϵ is emissivity of surface ($0 < \epsilon < 1$), T_s is absolute temperature on surface ($^\circ K$), T_{air} is ambient temperature ($^\circ K$), σ is Stefan-Boltzman constant ($5.67 \times 10^{-8} W/m^2 \cdot K^4$) and A_s is the specimens surface area (m^2).

Since the emissivity is varied based on the color of the object and all concrete specimens with different mix proportion produce mostly the similar gray color, thus the emissivity value in this study was selected to be 0.92. Then, thermal transient analysis was performed for 4 hours as in the actual test. Table 7 shows the summary of the inputs for the analysis.

Table 7. Inputs of boundary condition.

Inputs	Heating process: 0 - 120 min	Cooling process: 120 min - 240 min	References
Heating Flux	710 W/m ²	0 W/m ²	Back analysis
Convection coefficient	5.7 W/m ² .K	5.7 W/m ² .K	Duffie, et al 2013 [14]
Ambient temperature	Measured	Measured	Shown in Fig. 4

3.5. Numerical Simulation Modelling

3.5.1. FEM meshing

A 3-dimensional modelling was adopted in this simulation considering all related elements such as styrofoam, concrete, concrete modified layer, steel and rust thickness. Figure 6 shows the 3-D meshing of a test specimen surrounded by styrofoam. Noted that, concrete modified layer is the concrete zone above the reinforcing steel. The thermal properties of this concrete zone is modified. The modification is adopted based on the heterogeneity of concrete mix proportion caused by the uneven distribution of aggregate (in case of non-corroded specimen) and also the diffusion of ferrous ions into pores solutions of concrete above steel bar (in case of corroded specimen) as shown in Fig. 7. The finite elements meshing for this thermal analysis was adopted with 20-nodes elements hex dominant with a size of 5mm for styrofoam element, 5mm for concrete elements and 2mm for steel bar elements. Since rust thickness is very thin, meshing size is defined based on the estimated thickness of rust shown in Fig. 8.

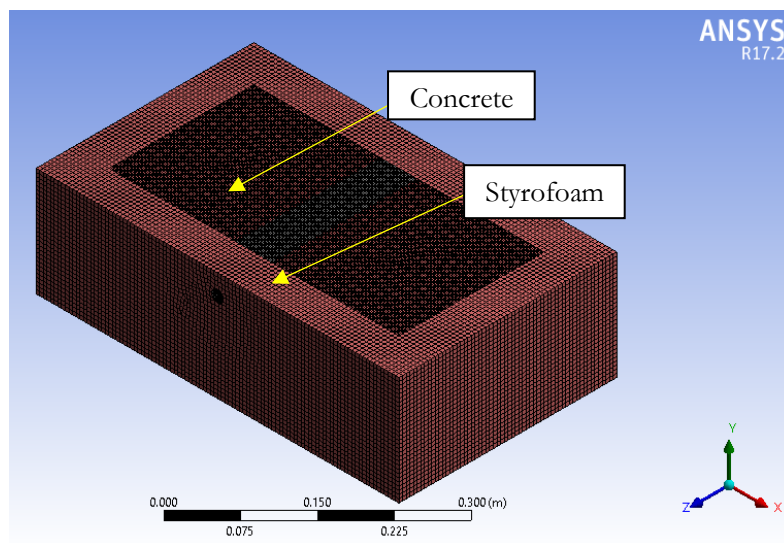


Fig. 6. 3-D modelling of a test specimen.

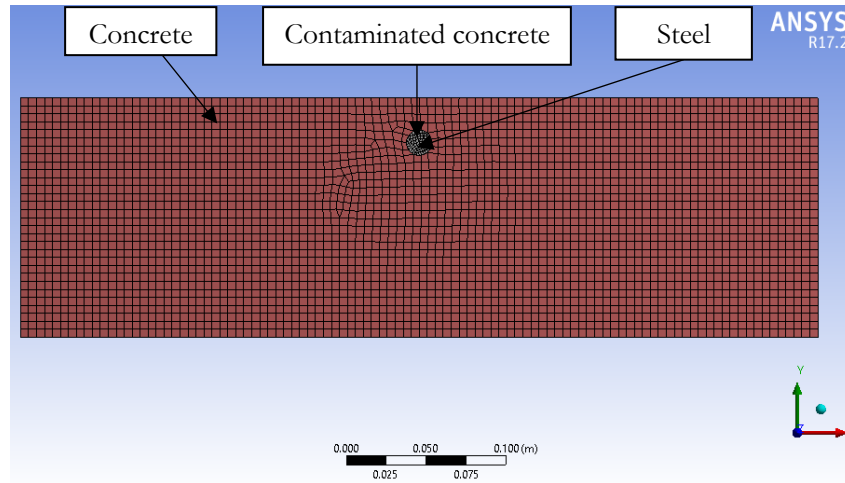


Fig. 7. Cross section of a simulation model.

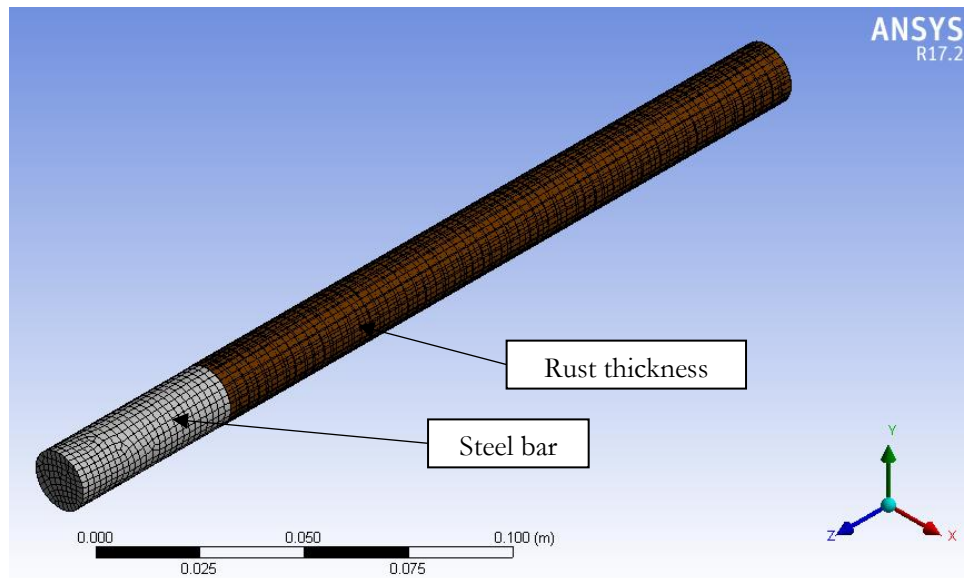


Fig. 8. Steel bar and rust thickness elements.

3.5.2. Initial and boundary conditions

The thermal load heat flux, heat convection and heat radiation are applied only on the top surface of the specimen as illustrated in Fig. 9. The detail of simulation input for heat convection and heat radiation are shown in Table 8.

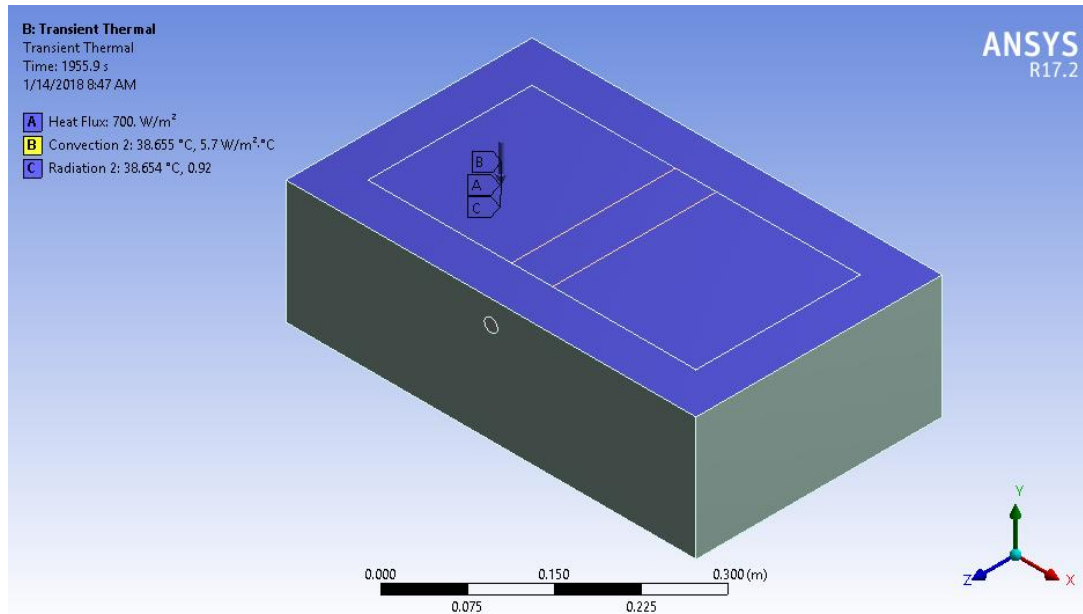


Fig. 9. The applied boundary conditions.

Table 8. Simulation input parameters for heat convection and heat radiation [14-16].

Parameters	Input
Convection coefficient, h_c	5.7 W/m ² .K
Emissivity, ϵ	0.92

3.6. Transient Thermal Analysis Process

To perform transient thermal analysis, it is necessary to apply thermal loading properly. Thus, based on the actual hypothesis and results of experimental work, back analysis can be implemented to precisely obtain the thermal loading as heat flux. Performing back calculation properly, the temperature rise of the tested specimens were used. Furthermore, the heating time, actual mass and surface area of the specimen were measured directly. Specific heat, on the other hand, was estimated by using prediction model of Choktaweekarn, (2009). Thus, from Eq. (8), heat flux can be calculated.

After obtaining all the required inputs, the thermal transient analysis can be performed. Firstly, this numerical simulation was applied to simulate the results of the specimen with no corrosion. This is aimed to verify the temperature profile at line S (side) since this side location have just concrete with constant thermal properties. In this study, the input parameters such as heat flux and thermal properties was adjusted to obtain the best fit temperature profiles with the experimental results. After fitting the simulation results with the results of specimen with no corrosion, the inputs initial and boundary conditions are kept the same for the analysis of the specimen with corrosion.

4. Results and Discussion

4.1. Effect of Concrete Mix Proportion

The results of temperature history of control specimens with different mix proportions are shown in Fig. 10. These results evidently clarify that with lower water to binder ratio, the temperature increases faster when compared to the case of higher water to binder ratio due to different thermal properties. This is confirmed with Choktaweekarn, et al. [8, 17].

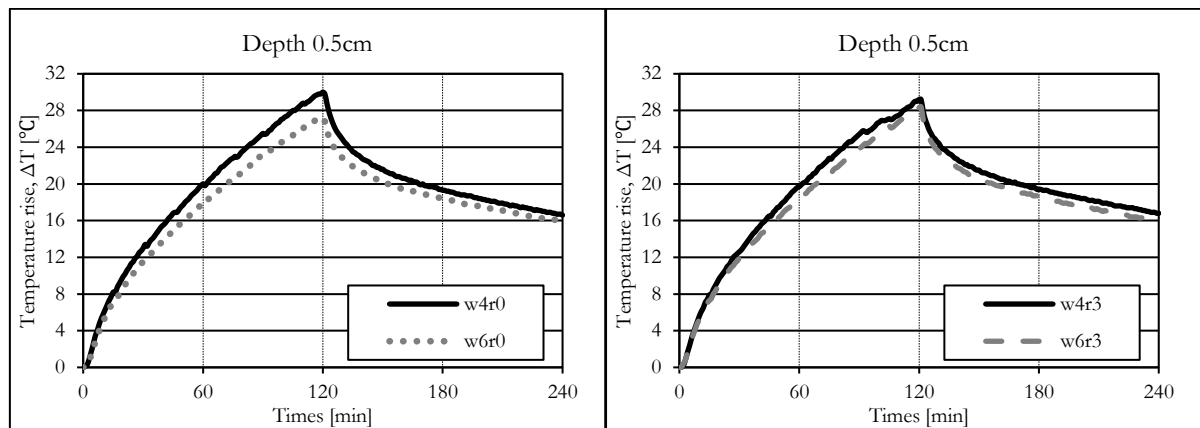


Fig. 10. Temperature history of mixtures with different water to binder ratio at depth 0.5 cm during heating and cooling.

Based on the prediction model of Choktaweekarn, et al. [8, 17], the estimated thermal properties of all tested mix concrete specimens are shown in Table 5. It is proved that the thermal conductivity of all specimens are almost equal since the mixtures share the same amount of aggregates. In contrast, the specific heat is significantly affected by water to binder ratio. As seen, the specific heat of mixture w4r0, with lower amount of water and porosity, is significantly lower than that of w6r0. This property is the main reason why temperature of the control specimen with w4r0 increases faster than w6r0. Lower specific heat leads to higher temperature for the same amount of heat input, so leads to higher temperature gradient and then faster heat transfer. On the other hands, fly ash replacement is seen to have less effect on thermal properties of concrete because specific heat changes slightly due to effect of fly ash as shown in Table 5.

4.2. Effect of Corrosion Amount

To be easier to observe the effect of corrosion on the thermal behavior of corroded specimen, the results of temperature rise are plotted for various target specimens. Furthermore, the different temperature between the specimens with and without corrosion (control) are also included. Figure 11 compares temperature history of specimen w4r0 at different depths between the control specimen with no corrosion and the specimen having corrosion amount (steel mass loss) of 3.05 mg/cm^2 .

As shown, there is no significant effect of corrosion at depth 0.5 and 1.5cm. However, at deeper part below the steel bar (at depth 4.1 cm and 7.5 cm), the temperature in the specimen with corrosion is higher than that of the specimen with no corrosion (about 0.8 and 0.2 °C, respectively). This is due to the fact that, the corrosion products obtained by the impressed currents method was formed and confined at the interfacial zone of steel and concrete which agreed well with the study of Caré, et al [18] and led to increasing of heat conductivity. This mechanism is also explained by the study of Michel et al. [19] which was focused on the corrosion induced cracking by X-ray attenuation measurement. The results of image analysis of x-ray attenuation measured by Michel, et al. presented the corrosion products, propagation of cracks and the diffusion of corrosion products into pore solution after initiation of accelerated corrosion test. The images clearly shown that corrosion products significantly formed at the interface of concrete and steel and induce crack. In addition, the study on thermal conduction mechanism of ferric oxide presented by Akiyama, et al. [20] shows that the thermal conductivity of ferric oxide is inversely proportional to its porosity. The lower percentage of rust porosity has the higher thermal conductivity. It was found from their study that when the porosity of ferrous oxide is lower than 45%, heat conductivity of rust layer is relatively higher when compared to conventional concrete but still largely lower than that of reinforcing steel. Thus, the results of this study is confirmed. When there is corrosion, dense rust, with high thermal conductivity, leads to faster heat transfer to the deeper part below the corroded steel bar.

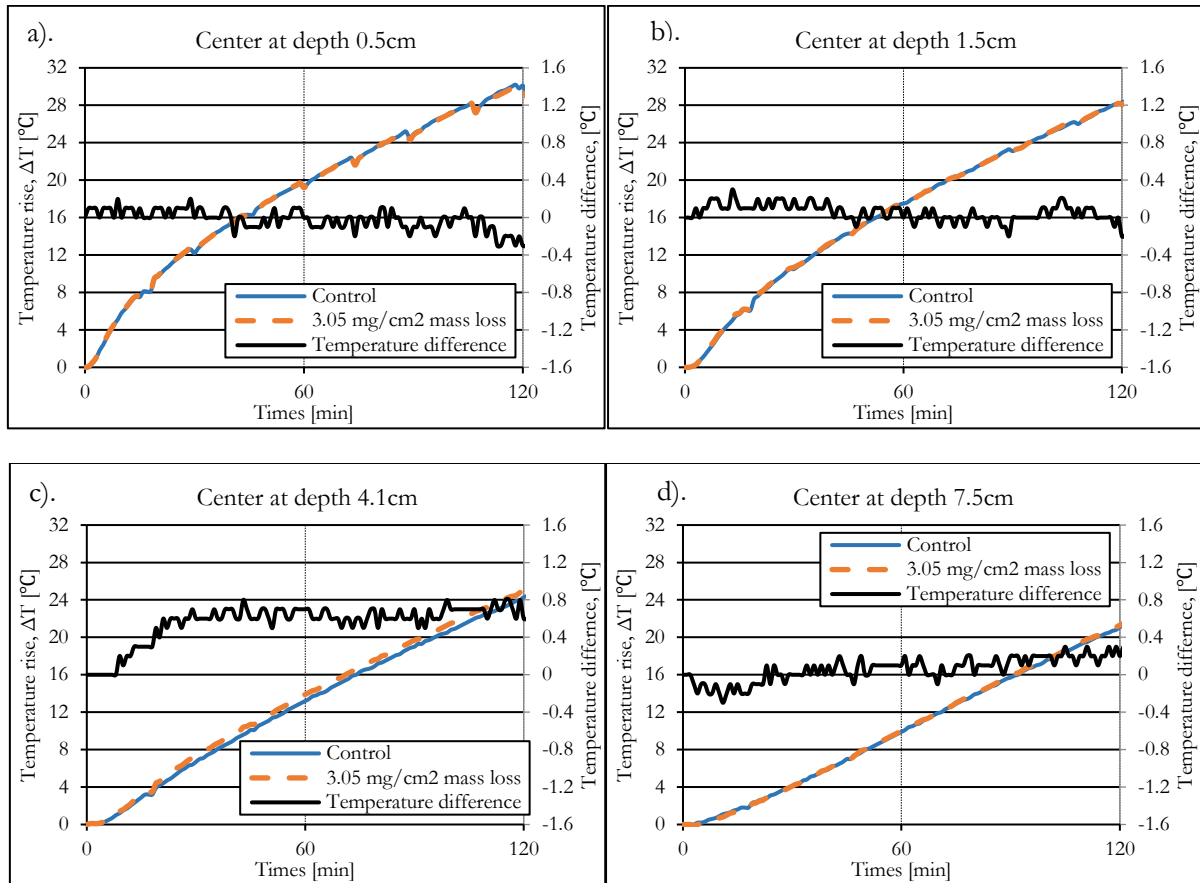


Fig. 11. Comparison of temperature history between w4r0 specimens without corrosion and with 3.05mg/cm² corrosion amount. a). at depth 0.5cm, b). at depth 1.5cm, c). at depth 4.1cm and d). at depth 7.5cm.

Furthermore, when the corrosion amount is larger, the temperature of corroded specimen is more significantly influenced as shown in Fig. 12. This result is obviously due to the fact that the higher amount of corrosion leads to the greater corrosion product layer. It was confirmed by backscattered electron (BSE) imaging analysis results of Wong, et al. [21]. The BSE images collectively proved that as the amount of corrosion increase the thickness of corrosion production accumulated at the steel concrete interface significantly is also larger. Specifically, in this study, when corrosion reaches 36.57 mg/cm² of mass loss, the thickness of rust estimated by Faraday's law is approximately 0.13977mm. This higher thickness of rust conduct the heat faster when compared to corrosion level of 3.05mg/cm². On the other hand, unlike small amount of corrosion product, higher corrosion amount is also observed to have effect on the thermal behavior at location above the rusted bar. This is because the corrosion products obtained from corrosion acceleration method diffuse into porous structure of top covering before it generates crack [18, 22, 23]. This study also confirmed to have diffusion of corrosion product filled in porous zone as shown in Fig. 13(a) and Fig. 13(b). Similarly, chloride ions are also mentioned to migrate into pore solution above reinforcing steel. Furthermore, the previous research on effect of chloride content on thermal properties of concrete [24] proved that chloride in pores reduces specific heat of the concrete. Thus, from the different temperature history obtained from the experimental work, it can be said that the presence of chloride and corrosion product penetrated into the concrete pores changes thermal properties of concrete by decreasing specific heat and increasing thermal conductivity.

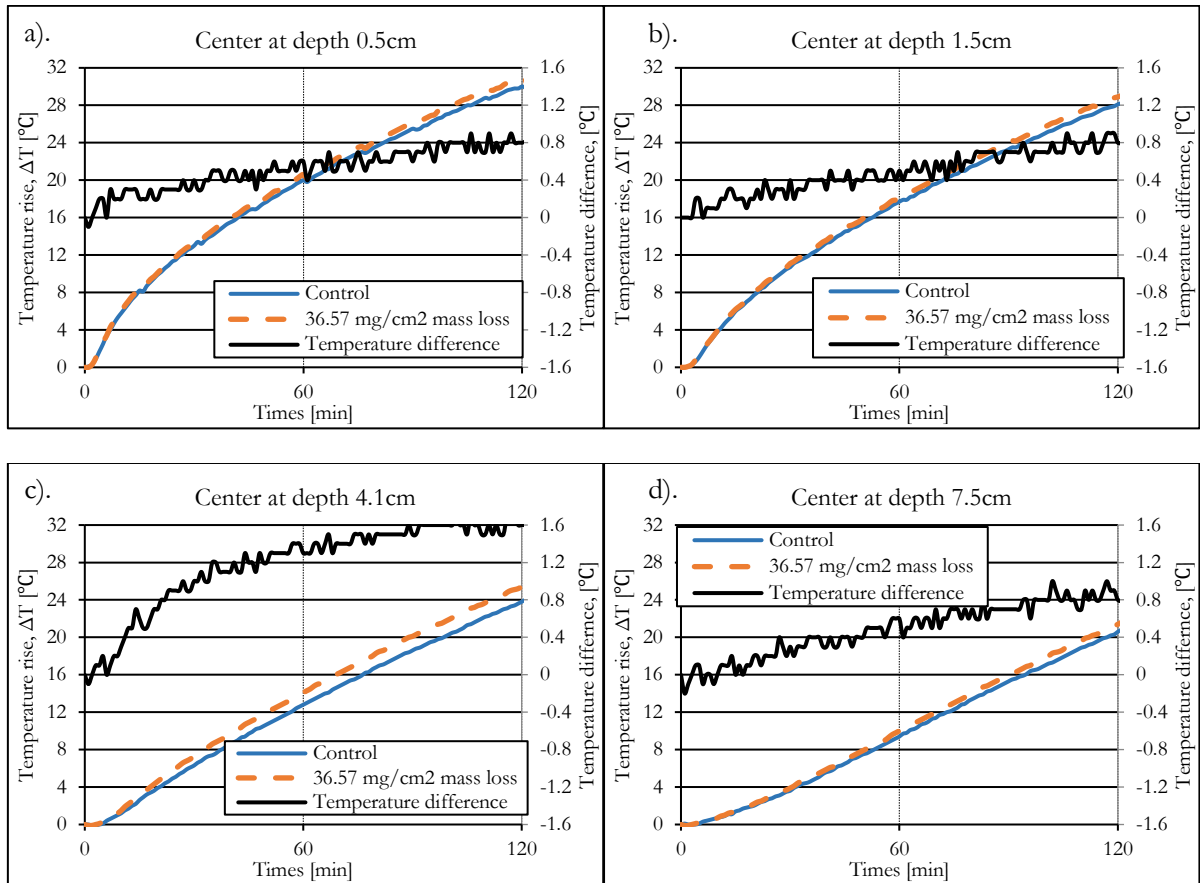


Fig. 12. Comparison of temperature history between w4r0 specimens without corrosion and with 36.57 mg/cm² corrosion amount. a). at depth 0.5cm, b). at depth 1.5cm, c). at depth 4.1cm and d). at depth 7.5cm.

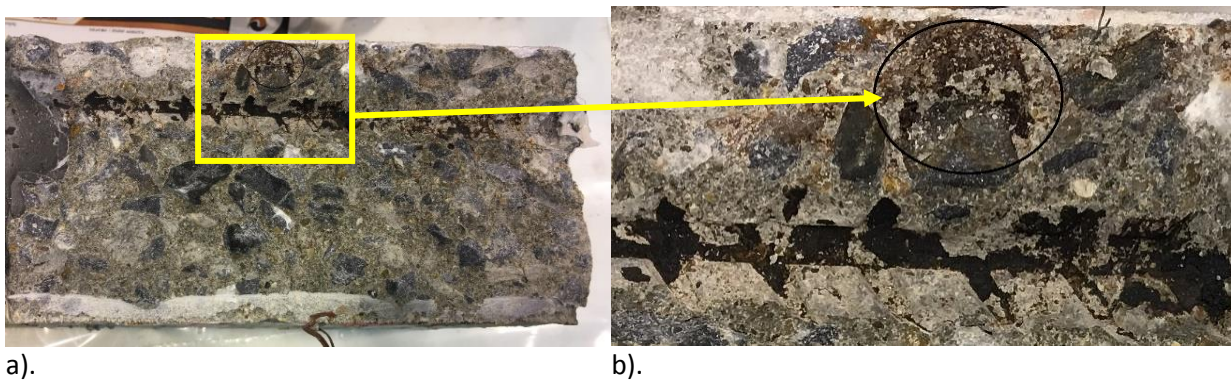


Fig. 13. a). Corrosion profile of corroded specimen. b). Presence of rust in concrete pores.

Figure 14 shows the temperature history of specimens at depth 0.5cm above the rusted bar of specimens w4r0 and w6r0 with a corrosion amount of 3.05 mg/cm². A good confirmation of this results was observed by the x-ray attenuation technique on the investigation of penetration depth of corrosion product by impressed current method, a study of Mihel, et al. [25]. As expected, the results of temperature differences between specimens with and with no corrosion prove that thermal behavior of corroded specimen is also influenced by concrete properties. As shown in Fig. 14 and Fig. 15, at the same amount of corrosion loss, the corroded w4r0 specimen tends to have lower temperature difference when compared to the corroded w6r0 specimen. Furthermore, as the amount of corrosion is higher, the temperature difference is more significant. The temperature of corroded w4r0 specimen is less affected by the corrosion products due to the fact that the w4r0 specimen, which is in contrast to w6r0, is denser and has lower porosity, resulting in lower chloride penetration as well as the diffusion of corrosion products into the concrete pores. These results cause higher

specific heat but lower heat conductivity in w4r0 specimen than in w6r0 specimen. The diffusion rate of chloride and corrosion products change with the concrete properties can be explained by the capillary pore structure which was confirmed to vary with water to binder ratio [26, 27].

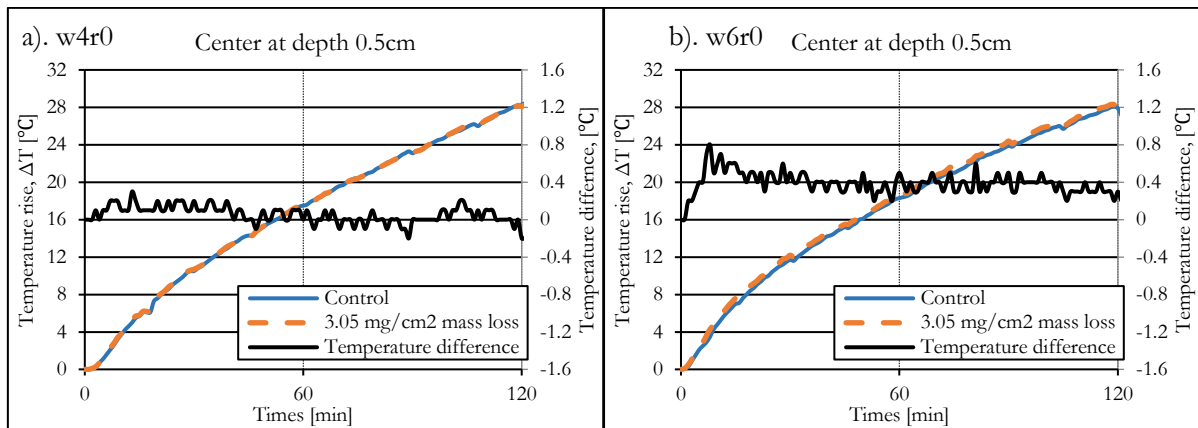


Fig. 14. Comparison of temperature history at depth 0.5cm of specimen with 3.05 mg/cm² corrosion amount and with no corrosion. a). specimen w4r0, b). specimen w6r0.

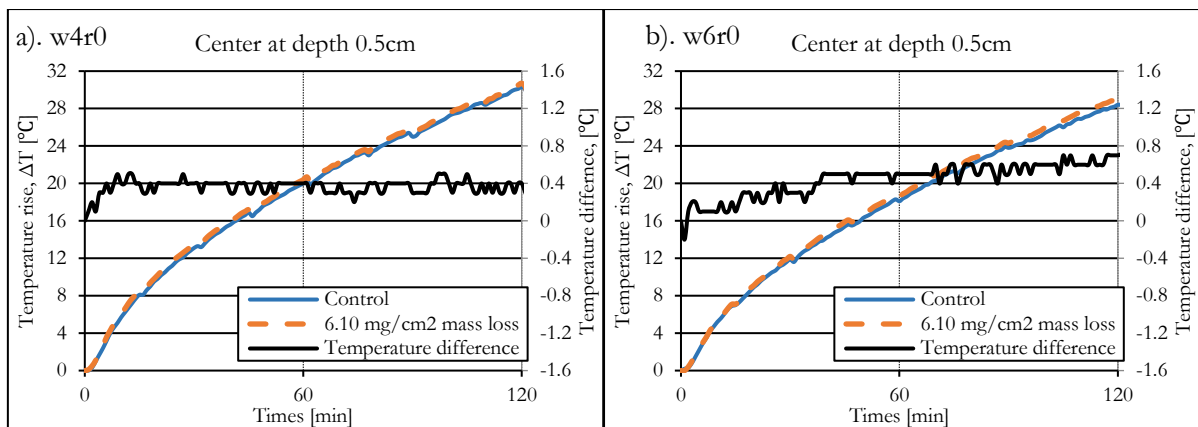


Fig. 15. Comparison of temperature history at depth 0.5cm of specimen with 6.10 mg/cm² corrosion amount and with no corrosion. a). specimen w4r0, b). specimen w6r0.

The summary of values of temperature difference in both w4r0 and w6r0 specimens at different corrosion amount (mass loss) are shown in Table 9 and also results of temperature differences at depth 0.5 cm are plotted in Fig. 16. As a comparison between w4r0 and w6r0 specimens at the same level of mass loss, the temperature difference of w4r0 tends to be lower than w6r0 at all measured depth. This is due to more penetration of corrosion products and chloride in pore structure causing lower specific heat but higher heat conductivity of w6r0 specimens. Except at the corrosion level of 36.57 mg/cm², cracks were generated on the top surface of w6r0 specimen. The cracks were fully filled with water which increased specific heat and lower the temperature difference. At higher corrosion mass loss, temperature difference tends to be higher due to penetration of corrosion products and chloride in pore structure both w4r0 and w6r0.

Table 9. Temperature difference at different depth of w4r0 and w6r0 specimens for different corrosion amount during heating process.

Depth	Mass loss									
	3.05 mg/cm ²		6.10 mg/cm ²		12.19 mg/cm ²		24.38 mg/cm ²		36.57 mg/cm ²	
	Temperature difference between corroded and non-corroded specimen (°C)									
	w4r0	w6r0	w4r0	w6r0	w4r0	w6r0	w4r0	w6r0	w4r0	w6r0
0.5cm	0	0.4	0.4	0.7	0.4	0.9	0	0.2	0.8	0.5
1.5cm	0	0.2	0.4	0.6	0	0.5	0	0.3	0.8	0.4
4.1cm	0.8	0.6	1.2	0.8	0.8	0.8	0.8	0.8	1.6	0.8
7.5cm	0.2	0.5	0.4	0.8	0.4	-	0.4	-	0.8	-

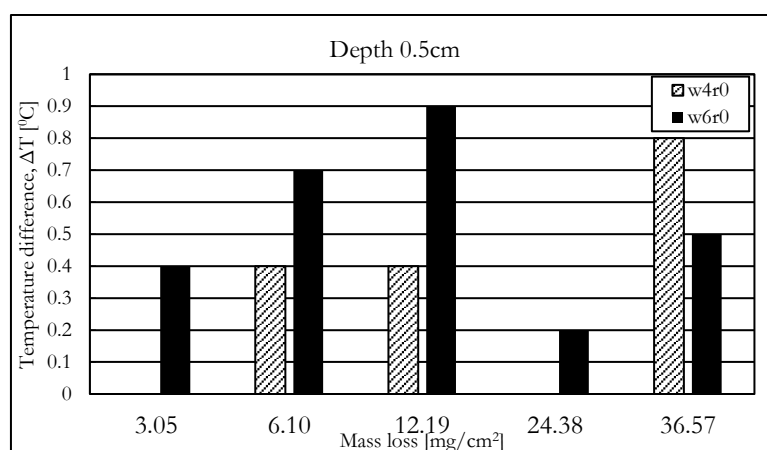


Fig. 16. Temperature differences at depth 0.5 cm in w4r0 and w6r0 specimens at different corrosion amount (mass loss).

4.3. Temperature Differences near the Surface between the Location above the Rusted Bar and Other Location

The purpose of this section is to check the possibility to detect corrosion of reinforcing steel before cracking by using thermography methods. Before the corrosion reached 1.16% of weight loss, all investigated reinforced concrete specimens were not found to have any cracks generated on the top surface.

Figure 17 shows temperature history and thermal contrast between line C, center, and line S, side, at the depth 0.5cm of w6r0 specimen. Fig. 17(a) is for the control specimen with no corrosion and Fig. 17(b) is for that with 3.05 mg/cm² corrosion amount. These results are used to confirm the thermal contrast and the possibility to observe the different temperature pattern on the surface by the effect of corrosion of reinforcing steel. As seen, during the heating process, the results obtained from the thermocouples show that the temperature at the position above the rust (center) is higher than that at another position (side) with an approximate difference of 2°C for specimen with no corrosion and 3°C for specimen with 3.05mg/cm² corrosion. The differences in the no corrosion specimens is caused by the non-uniformity of concrete where less coarse aggregate content is expected above the steel bar due to small cover depth. At the center position above the steel bar is expected to have less coarse aggregate content. Thus, its thermal properties (like properties of mortar) are likely to have higher specific heat and lower thermal conductivity when compared to concrete. It should be noted that the specific heat of mortar is 978.99 J/kg.°C and thermal conductivity is 1.507 W/m.°C while specific heat of concrete is 913.978 J/kg.°C and thermal conductivity is 2.321 W/m.°C. Even though at the center position has high specific heat but with its low thermal conductivity, the heat is accumulated and slowly conducted further. Thus, it results in high temperature history. However, thermal contrast of specimen with 3.05mg/cm² corrosion amount is seen to be more significant due to effect of chloride and corrosion products.

On the other hand, the IR camera was also used to capture the thermal image of the tested specimens. From the thermography, the surface temperature are obviously uniformed. Thus, it was hardly observed any

different thermal pattern due to the present of corrosion. As shown in Fig. 18, at the end of heating and cooling process, the thermal image shows that temperature just above area with presence of corroded steel (SP1, center) is almost equal to the temperature above area without steel (SP2, side). Thus, there is no any significant hot spot or cool spot was observed. This may be due to the non-uniformity of moisture affecting surface temperature of concrete no only the corrosion of reinforcing steel.

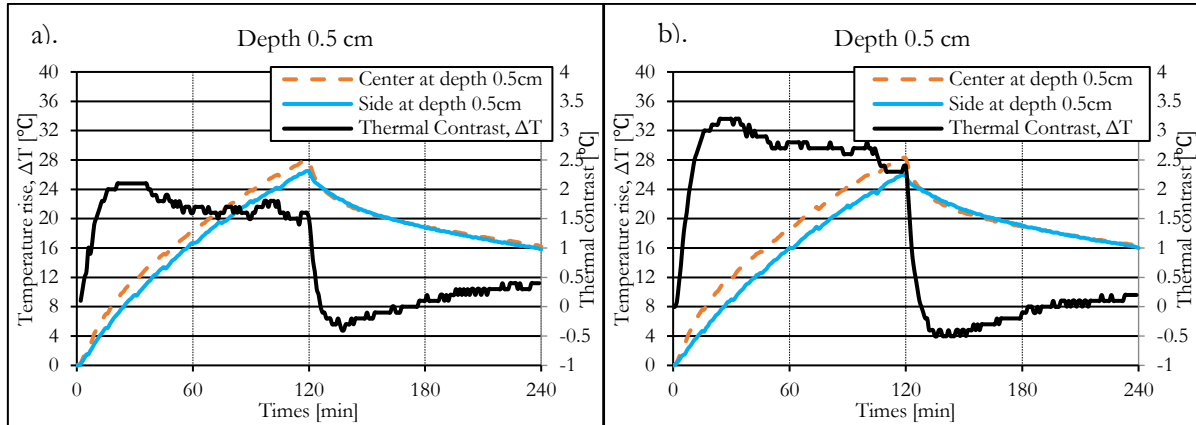


Fig. 17. Temperature history and thermal contrast at depth 0.5cm of specimen w6r0. a). No corrosion, b). with 3.05mg/cm² corrosion amount.

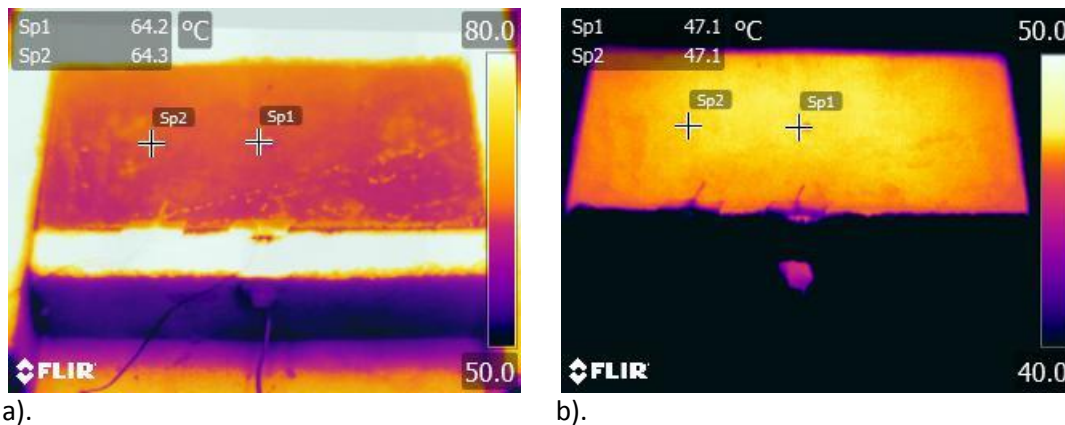


Fig. 18. Thermal picture of tested specimen w6r0 with 24.38mg/cm². a). 120 min after heating, b). 120 min after cooling process.

4.4. Numerical Simulation

This numerical simulation is used to confirm some mechanism explained in the part of experimental results. The analytical results from Fig. 19 to Fig. 20 show that the estimated values of temperature at all depths have similar tendencies with the experimental results. Figures 19 and 20 compare the experimental results with the simulated results at each depth of the non-corroded w6r0 specimen as an example. It is noted that not all simulated results are presented here for making the paper concise.

As seen, at the side position, the temperature history obtained from numerical simulation and experiment are in a good agreement. On the other hands, at the center part with the presence of reinforcing steel, the numerical simulation results are lower than those of the experiment. This is expected to be caused by the heterogeneity of concrete where there is less coarse aggregate above the reinforcing steel. Numerical simulation provides quite good results in the area closing to the concrete top surface (depth 0.5cm and 1.5cm) and the accuracy of the estimated temperature is within 2%-5% of the experimental results. To improve the precision of simulation, the effect of chloride and corrosion products on thermal behavior of concrete is required for future improvement.

5. Conclusions

The results obtained from the experiments in study can be concluded that:

At the low percentage of weight loss, the presence of rust formed by impressed current method has a slight effect on thermal behavior of reinforced concrete specimens. The dense rust with high heat conduction influence the temperature at the position below corroded bars rather than position above corroded bar.

On the other hand, when corrosion amount increases, the temperature of corroded reinforced concrete specimen is seen to significantly affected at both positions, above and below the rusted bar. This is because corrosion product was found to penetrate into pores structure of concrete cover. This behavior is in agreement with other study and it is believed that the diffused chloride and corrosion product modify the thermal properties of concrete by reducing its specific heat about 5% but increasing its thermal conductivity about 3%.

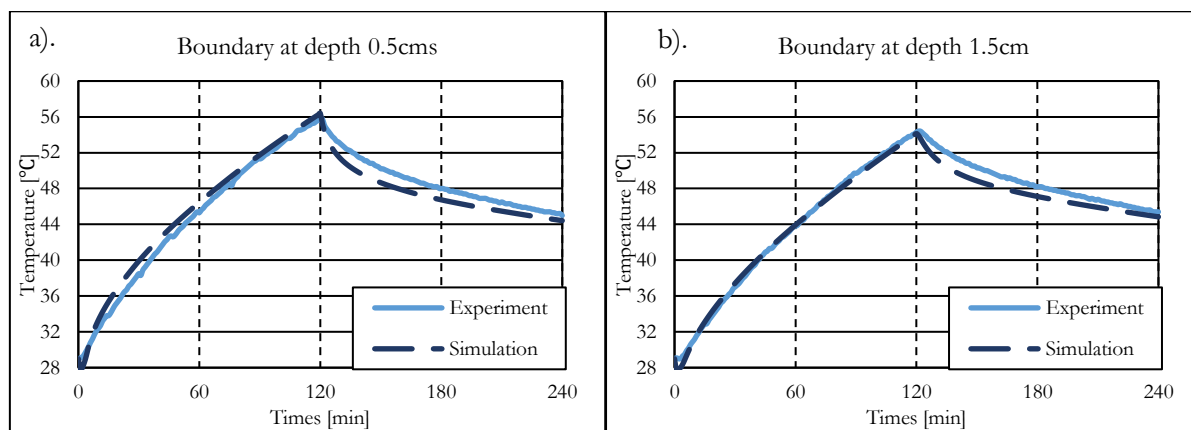
The effect of chloride and corrosion greatly influenced the thermal behavior of concrete with high water to binder ratio due to the fact that higher water to binder ratio generate greater porosity in which chloride and corrosion product can penetrate into the pores more easily.

The estimated temperature history at all depths obtained from the simulation are confirmed to have similar tendencies with the experimental results. However, the results of numerical simulation were still not precisely fit with the experimental results. The numerical simulation of the effect of chloride and corrosion product on thermal behavior of concrete will be extended in our future study.

To improve the detectability of corrosion of reinforcing steel by thermography, it can be probably recommended the application of thermograph combined with the method of Induction heating. This technique can possibly be more effective because the heating method will heat directly the corroded steel in side concrete. This may cause better difference of concrete surface temperature due to corrosion of reinforcing steel. However, concern should be given on heated temperature does not affect properties of steel and concrete. Temperature of heating less than 70°C is recommended.

Acknowledgement

The author would like to acknowledge the Center of Excellence in Material Science, Construction and Maintenance Technology project, Thammasat University. Moreover, acknowledgements are granted to the Ministry of Education of Thailand and ASEA-UNINET scholarship for providing scholarship to Cambodian students to pursue higher education in Thailand.



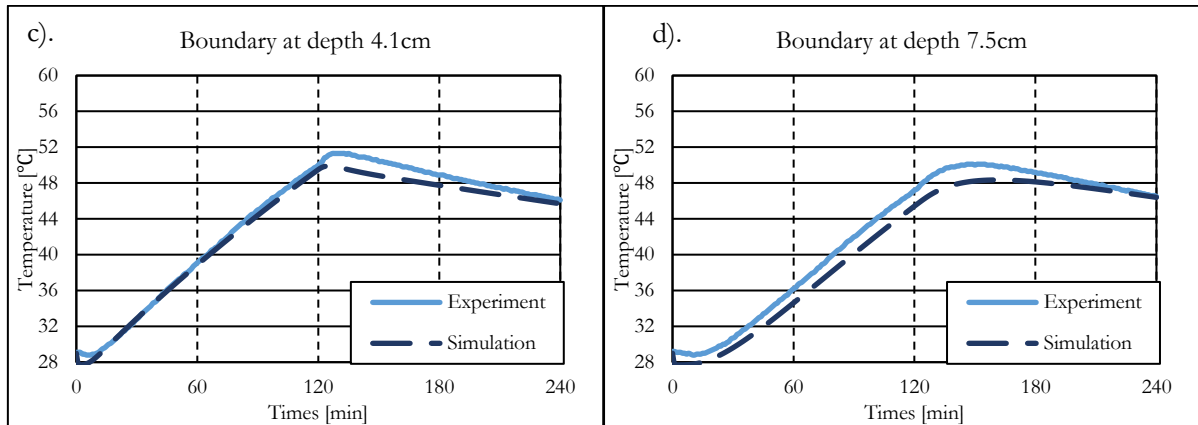


Fig. 19. Comparison of temperature history of non-corroded specimen with w6r0 at line S (side position) between experiment and simulation, a). at depth 0.5cm, b). at depth 1.5cm, c). at depth 4.1cm and d). at depth 7.5cm.

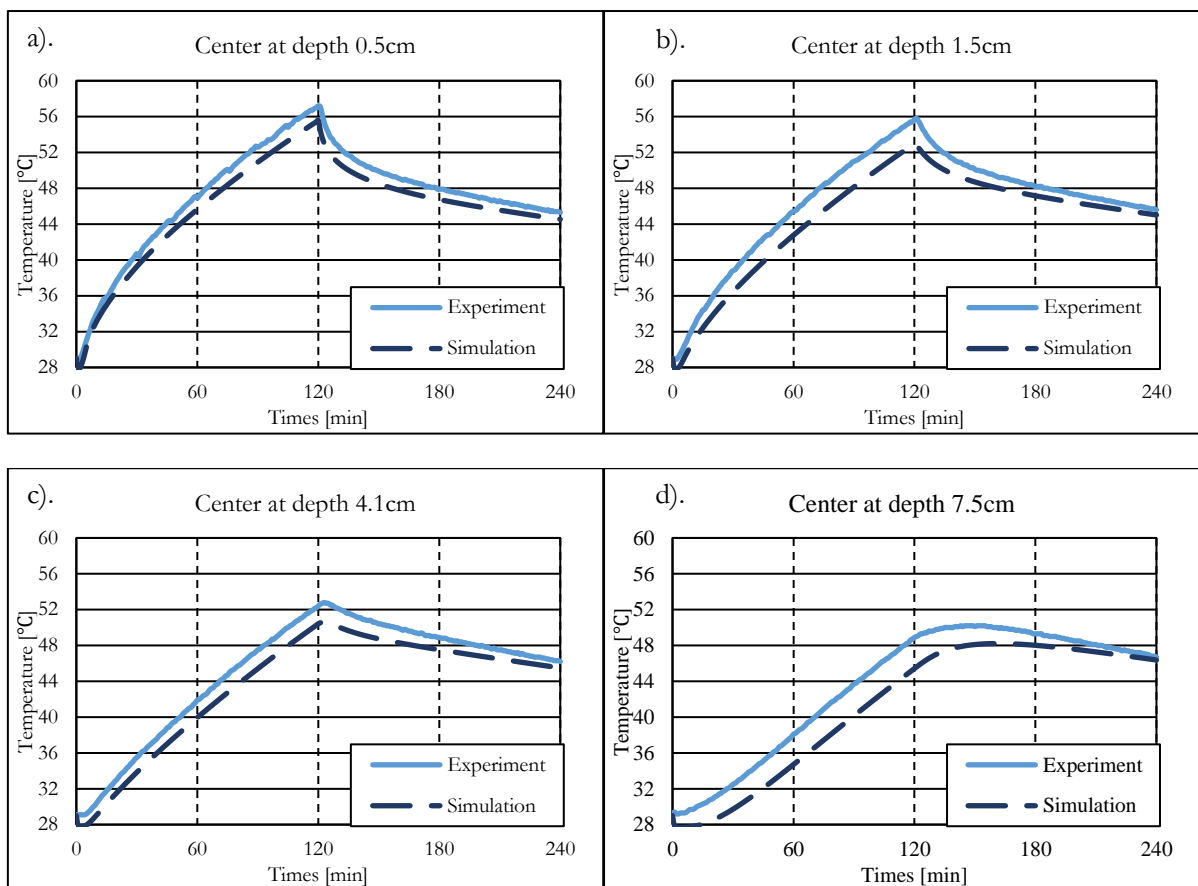


Fig. 20. Comparison of temperature history of non-corroded specimen with w6r0 at line C (center position) between experiment and simulation, a). at depth 0.5cm, b). at depth 1.5cm, c). at depth 4.1cm and d). at depth 7.5cm.

6. Acknowledgements

The author would like to acknowledge the Center of Excellence in Material Science, Construction and Maintenance Technology project, Thammasat University. Moreover, acknowledgements are granted to the Ministry of Education of Thailand and ASEA-UNINET scholarship for providing scholarship to Cambodian students to pursue higher education in Thailand.

References

- [1] J. P. Broomfield, *Corrosion of Steel in Concrete: Understanding, Investigation and Repair*. CRC Press, 2002.
- [2] U. Angst, B. Elsener, C. K. Larsen, and Ø. Vennesland, "Critical chloride content in reinforced concrete—A review," *Cement and Concrete Research*, vol. 39, pp. 1122-1138, 2009.
- [3] ASTM, "Test method for half-cell potentials of uncoated reinforcing steel in concrete," C876-91R99, 1991.
- [4] M. El-Reedy, *Steel-Reinforced Concrete Structures: Assessment and Repair of Corrosion*. CRC Press, 2007.
- [5] S. Bagavathiappan, B. B. Lahiri, T. Saravanan, J. Philip, and T. Jayakumar, "Infrared thermography for condition monitoring – A review," *Infrared Physics & Technology*, vol. 60, pp. 35-55, Sept. 2013.
- [6] C. Maierhofer, R. Arndt, and M. Röllig, "Influence of concrete properties on the detection of voids with impulse-thermography," *Infrared Physics & Technology*, vol. 49, pp. 213-217, Jan. 2007.
- [7] T. A. El Maaddawy and K. A. Soudki, "Effectiveness of impressed current technique to simulate corrosion of steel reinforcement in concrete," *Journal of Materials in Civil Engineering*, vol. 15, pp. 41-47, 2003.
- [8] P. Choktawekarn, W. Saengsoy, and S. Tangtermsirikul, "A model for predicting the specific heat capacity of fly-ash concrete," *ScienceAsia*, vol. 35, no. 2, pp.178-182, 2009.
- [9] H. Oshita, H. Horie, S. Nagasaka, O. Taniguchi, and S. Yoshikawa, "Nondestructive evaluation of corrosion in reinforced concrete by thermal behavior on concrete surface due to electro-magnetic heating," *JSCCE*, vol. 65, no. 1, pp. 76-92, 2009.
- [10] M. J. Moran, H. N. Shapiro, B. R. Munson, and D. P. DeWitt, "Introduction to thermal systems engineering," *Thermodynamics, Fluid Mechanics, and Heat Transfer*. John Wiley & Sons, 2003.
- [11] J. Castoreña, F. Almeraya-Calderon, J. Velásquez, C. Gaona-Tiburcio, A. Cárdenas, C. Barrios-Durstewitz, L. L. León, and A. Martínez-Villafane, "Modeling the time-to-corrosion cracking of reinforced concrete structures by finite element," *Corrosion*, vol. 64, pp. 600-606, 2008.
- [12] C. Andrade, C. Alonso, and F. Molina, "Cover cracking as a function of bar corrosion: Part I- Experimental test," *Materials and Structures*, vol. 26, pp. 453-464, 1993.
- [13] D. Qiao, H. Nakamura, Y. Yamamoto, and T. Miura, "Crack patterns of concrete with a single rebar subjected to non-uniform and localized corrosion," *Construction and Building Materials*, vol. 116, pp. 366-377, 2016.
- [14] J. A. Duffie and W. A. Beckman, *Solar Engineering of Thermal Processes*. John Wiley & Sons, 2013.
- [15] R. Faria, M. Azenha, and J. A. Figueiras, "Modelling of concrete at early ages: Application to an externally restrained slab," *Cement and Concrete Composites*, vol. 28, pp. 572-585, 2006.
- [16] Y. Cengel and A. Ghajar, *Heat and Mass Transfer: Fundamentals and Applications + EES DVD for Heat and Mass Transfer*. McGraw-Hill Education, 2010.
- [17] P. Choktawekarn, W. Saengsoy, and S. Tangtermsirikul, "A model for predicting thermal conductivity of concrete," *Magazine of Concrete Research*, vol. 61, pp. 271-280, 2009.
- [18] S. Caré, Q. T. Nguyen, V. L'Hostis, and Y. Berthaud, "Mechanical properties of the rust layer induced by impressed current method in reinforced mortar," *Cement and Concrete Research*, vol. 38, pp. 1079-1091, 2008.
- [19] A. Michel, B. J. Pease, M. R. Geiker, H. Stang, and J. F. Olesen, "Monitoring reinforcement corrosion and corrosion-induced cracking using non-destructive x-ray attenuation measurements," *Cement and Concrete Research*, vol. 41, pp. 1085-1094, 2011.
- [20] T. Akiyama, H. Ohta, R. Takahashi, Y. Waseda, and J.-i. Yagi, "Measurement and modeling of thermal conductivity for dense iron oxide and porous iron ore agglomerates in stepwise reduction," *ISIJ International*, vol. 32, pp. 829-837, 1992.

- [21] H. S. Wong, Y. X. Zhao, A. R. Karimi, N. R. Buenfeld, and W. L. Jin, "On the penetration of corrosion products from reinforcing steel into concrete due to chloride-induced corrosion," *Corrosion Science*, vol. 52, pp. 2469-2480, 2010.
- [22] G. Nossoni and R. S. Harichandran, "Electrochemical-mechanistic model for concrete cover cracking due to corrosion initiated by chloride diffusion," *Journal of Materials in Civil Engineering*, vol. 26, p. 04014001, 2011.
- [23] D. V. Val, L. Chernin, and M. G. Stewart, "Experimental and numerical investigation of corrosion-induced cover cracking in reinforced concrete structures," *Journal of Structural Engineering*, vol. 135, pp. 376-385, 2009.
- [24] D. Im, P. Sanchaen, P. Julnipayawong, and S. Tangtermsirikul, "Effects of chloride content on thermal properties of concrete," *International Journal of GEOMATE*, vol. 14, pp. 135-142, 2018.
- [25] A. Michel, B. J. Pease, A. Peterová, M. R. Geiker, H. Stang, and A. E. A. Thybo, "Penetration of corrosion products and corrosion-induced cracking in reinforced cementitious materials: Experimental investigations and numerical simulations," *Cement and Concrete Composites*, vol. 47, pp. 75-86, 2014.
- [26] D. P. Bentz and E. J. Garboczi, "Percolation of phases in a three-dimensional cement paste microstructural model," *Cement and Concrete Research*, vol. 21, pp. 325-344, 1991.
- [27] X. Chen and S. Wu, "Influence of water-to-cement ratio and curing period on pore structure of cement mortar," *Construction and Building Materials*, vol. 38, pp. 804-812, 2013.